A TEMPERATURE AND ABUNDANCE RETRIEVAL METHOD FOR EXOPLANET ATMOSPHERES

N. MADHUSUDHAN[1] AND S. SEAGER[1,2]
[1] Department of Physics and Kavli Institute for Astrophysics and Space Research, MIT, Cambridge, MA 02139, USA; nmadhu@mit.edu
[2] Department of Earth, Atmospheric, and Planetary Sciences, MIT, Cambridge, MA 02139, USA

ABSTRACT

We present a new method to retrieve molecular abundances and temperature profiles from exoplanet atmosphere photometry and spectroscopy. We run millions of one-dimensional (1D) atmosphere models in order to cover the large range of allowed parameter space. In order to run such a large number of models, we have developed a parametric pressure–temperature (P–T) profile coupled with line-by-line radiative transfer, hydrostatic equilibrium, and energy balance, along with prescriptions for non-equilibrium molecular composition and energy redistribution. The major difference from traditional 1D radiative transfer models is the parametric P–T profile, which essentially means adopting energy balance only at the top of the atmosphere and not in each layer. We see the parametric P–T model as a parallel approach to the traditional exoplanet atmosphere models that rely on several free parameters to encompass unknown absorbers and energy redistribution. The parametric P–T profile captures the basic physical features of temperature structures in planetary atmospheres (including temperature inversions), and fits a wide range of published P–T profiles, including those of solar system planets. We apply our temperature and abundance retrieval method to the atmospheres of two transiting exoplanets, HD 189733b and HD 209458b, which have the best *Spitzer* and *Hubble Space Telescope* data available. For HD 189733b, we find efficient day–night redistribution of energy in the atmosphere, and molecular abundance constraints confirming the presence of H_2O, CO, CH_4, and CO_2. For HD 209458b, we confirm and constrain the dayside thermal inversion in an average 1D temperature profile. We also report independent detections of H_2O, CO, CH_4, and CO_2 on the dayside of HD 209458b, based on six-channel *Spitzer* photometry. We report constraints for HD 189733b due to individual data sets separately; a few key observations are variable in different data sets at similar wavelengths. Moreover, a noticeably strong CO_2 absorption in one data set is significantly weaker in another. We must, therefore, acknowledge the strong possibility that the atmosphere is variable, both in its energy redistribution state and in the chemical abundances.

Key words: methods: numerical – planetary systems – planets and satellites: general – planets and satellites: individual (HD 209458b, HD 189733b) – radiative transfer

1. INTRODUCTION

Major advances in the detection and characterization of extrasolar planet atmospheres have been made during the last decade. Over a dozen hot Jupiter atmospheres have been observed by the *Spitzer Space Telescope* and a handful by the *Hubble Space Telescope* (*HST*). These observations have changed the field of exoplanets, enabling for the first time studies of atmospheres of distant worlds.

Observational highlights include the identification of molecules and atoms, and signatures of thermal inversions. *HST* observed water vapor and methane in transmission in HD 189733b (Swain et al. 2008b). Water vapor was also inferred in transmission at the 3.6 μm, 5.8 μm, and 8 μm in HD 189733b (Tinetti et al. 2007; but cf. Desert et al. 2009; and also Beaulieu et al. 2009). Water was inferred on the dayside of HD 189733b from the planet-star flux contrast in the 3.6–8.0 μm *Spitzer* broadband photometry (Barman 2008; Charbonneau et al. 2008). Additionally, Grillmair et al. (2008) reported a high signal-to-noise spectrum of the dayside of HD 189733b in the 5–14 μm range, using the *Spitzer* Infrared Spectrograph (IRS), and reported detection of water. More recently, *HST* detected carbon dioxide in thermal emission in HD 189733b (Swain et al. 2009a), in 1.4–2.6 μm. Previously, sodium was detected in HD 209458b (Charbonneau et al. 2002) and HD 189733b (Redfield et al. 2008). Several observations of the planetary dayside have also been reported for HD 209458b, first observed by *Spitzer* at 24 μm (Deming et al. 2005; Seager et al. 2005). A major observational discovery was the finding of strong emission features in the broadband

photometry of HD 209458b at secondary eclipse (Knutson et al. 2008), implying a thermal inversion in the atmosphere (Burrows et al. 2007, 2008). In tandem with our present work, water, methane, and carbon dioxide were independently inferred and recently reported on the dayside of HD 209458b, with *HST* NICMOS and five-channel *Spitzer* photometry (Swain et al. 2009b). Additionally, there are hints that variability of hot Jupiter thermal emission may be common (Knutson et al. 2007 versus Charbonneau et al. 2008; Charbonneau et al. 2008 versus Grillmair et al. 2008; Deming et al. 2005 versus D. Deming 2009, private communication). The discoveries of atmospheric constituents and temperature structures mark the remarkable successes of exoplanet atmosphere models in interpreting the observations.

Despite the successes of model interpretation of data, major limitations of traditional self-consistent atmosphere models are becoming more and more apparent. Model successes include the detection of thermal inversions on the dayside of hot Jupiters (Burrows et al. 2007; Knutson et al. 2008), and subsequent classification of systems on the same basis (Burrows et al. 2008; Fortney et al. 2008; Seager et al. 2008). The nature of the absorbers causing the inversions, however, is not yet known (Knutson et al. 2008, 2009b), forcing modelers to use an ad hoc opacity source to explain the data. The initially favored opacity sources, TiO and VO, may be unlikely to cause inversions of the observed magnitude (Spiegel et al. 2009).

A second model limitation arises because one-dimensional (1D) radiative-convective equilibrium models cannot include the complex physics involved in hydrodynamic flows. Existing models use a parameterization of energy transfer from the day-

side to night side (e.g., Burrows et al. 2008), using parameters for the locations of energy sources and sinks, and for the amount of energy transported.

One further example of atmospheric model limitations involves the treatment of chemical compositions. Self-consistent models generally calculate molecular mixing ratios based on chemical equilibrium along with the assumption of solar abundances, or variants thereof (e.g., Seager et al. 2005). However, hot Jupiter atmospheres should host manifestly non-equilibrium chemistry (e.g., Liang et al. 2003; Cooper & Showman 2006), which render the assumption of chemical equilibrium only a fiducial starting point.

With parameters used to cover complicated or unknown physics or chemistry, existing "self-consistent" radiative–convective equilibrium models are no longer fully self-consistent. Furthermore, given the computational time of such models, only a few models are typically published to interpret the data, often only barely fitting the data—a quantitative measure of fit is typically absent in the literature. In an ideal world, one would construct fully self-consistent 3D atmosphere models (e.g., Showman et al. 2009) that include hydrodynamic flow, radiative transfer, cloud microphysics, photochemistry, and non-equilibrium chemistry, and run such models over all of parameter space anticipated to be valid. Such models will remain idealizations until computer power improves tremendously, given that atmospheric circulation models can take weeks to months to run even with simple radiative transfer schemes.

We are motivated to develop a data-interpretation framework for exoplanet atmospheres that enables us to run millions of models in order to constrain the full range of pressure–temperature (P–T) profiles and abundance ranges allowed by a given data set. In this work, we report a new approach to 1D modeling of exoplanet atmospheres. Taking a cue from parameterized physics already being adopted by existing models, we go much further by parameterizing the P–T profile as guided by basic physical considerations and by properties of P–T profiles of planetary atmospheres in the literature. Indeed, it appears at present, the only way to be able to run enough models to constrain the P–T structure and abundances is to use a parameterized P–T profile. The essential difference between our new method and currently accepted radiative–convective equilibrium models is in the treatment of energy balance. We ensure global energy balance at the top of the atmosphere, whereas conventional atmosphere models use layer-by-layer energy balance by way of radiative and convective equilibrium. Our new method can be used as a stand-alone model, or it can be used to identify the parameter space in which to run a reasonable number of traditional model atmospheres. We call our method "temperature and abundance retrieval" of exoplanet atmospheres.

Atmospheric temperature and abundance retrieval is not new (e.g., Goody & Yung 1989). Studies of planetary atmospheres in the solar system use temperature retrieval methods, but in the present context there is one major difference. Exquisite data for solar system planet atmospheres means a fiducial P–T profile can be derived. The temperature retrieval process for atmospheres of solar system planets therefore involves perturbing the fiducial temperature profile. For exoplanets, where data are inadequate, there is no starting point to derive a fiducial model. Nevertheless, Swain et al. (2008b, 2009a) used previously published model P–T profiles of HD 189733b, and varied molecular abundances to report model fits to *HST* NICMOS spectra of HD 189733b. In another study, Sing et al. (2008) used a parametric temperature profile with a thermal inversion, and parameterized abundances,

required specifically to explain *HST* STIS optical observations of HD 209458b. Our model, however, is completely general in the choice of P–T profiles, ranges over tens of thousands of profiles, and satisfies the physical constraints of global energy balance and hydrostatic equilibrium. Our model reports, with contour plots, the quantitatively allowed ranges of P–T profiles and molecular abundances. In addition, we also report constraints on the albedo and day–night energy redistribution, and on the effective temperature.

In this paper, the P–T profiles are introduced in Section 2, and the radiative transfer model and parameter space search strategy are described in Section 3. Results of data interpretation with the model are presented in Section 4 for HD 189733b, and in Section 5 for HD 209458b. Section 6 discusses the overall approach, and prospects for future work. And, in Section 7 we present a summary of our results and conclusions.

2. TEMPERATURE–PRESSURE STRUCTURE

Our goal is to introduce a new method of parameterizing 1D models of exoplanetary atmospheres. Our approach is to parameterize the P–T profiles, instead of separately parameterizing each of the different physical processes that contribute to the P–T profiles. In what follows, we will first review the basic physics behind the temperature structure of planetary atmospheres which serves as motivation for our P–T form. Next, we will describe our parametric P–T profile. Finally, we compare our model P–T profiles with published profiles for some known planetary systems.

2.1. Temperature Structure in Planetary Atmospheres

The P–T profiles of planetary atmospheres are governed by basic physics. Here, we qualitatively describe the physics and shape of a representative P–T profile starting from the bottom of the atmosphere. We focus on the generality that the temperature structure at a given altitude depends on the opacity at that altitude, along with density and gravity.

In the deepest layers of the planet atmosphere, convection is the dominant energy transport mechanism. The high pressure (equivalently, high density) implies a high opacity, making energy transport by convection a more efficient energy transport mechanism than radiation. For hot Jupiters, the day-side radiative–convective boundaries usually occur at the very bottom layers of the atmospheres, at pressures higher than $\sim$100 bar. In the layers immediately above this boundary, the optical depth is still high enough that the diffusion approximation of radiative transport holds. The diffusion approximation, and the incident stellar flux predominantly absorbed higher up in the atmosphere, lead to a nearly isothermal temperature structure in the layers immediately above the radiative–convective boundary in hot Jupiters. It is assumed here that the energy sources in the planet interior are weak compared to the stellar irradiation. In the solar system giant planet atmospheres (and cooler exoplanet atmospheres as yet to be observed), the radiative–convective boundary occurs at lower pressures in the planet atmosphere than for hot Jupiters.

Above the isothermal diffusion layer, i.e., at lower pressures, the atmosphere becomes optically thin and the diffusion approximation breaks down. These optically thin layers are at altitudes where thermal inversions can be formed, depending on the level of irradiation from the parent star and the presence of strong absorbing gases or solid particles. Thermal inversions, or "stratospheres," are common to all solar system planets and
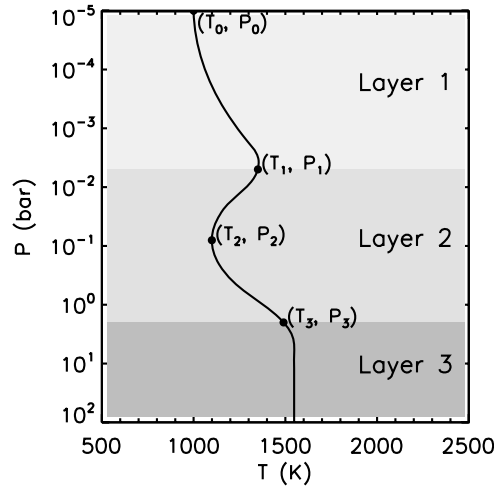
Figure 1. Parametric pressure–temperature (P–T) profile. In the general form, the profile includes a thermal inversion layer (Layer 2) and has six free parameters, see Equation (2). For a profile with thermal inversion, $P_2 > P_1$, and for one without a thermal inversion, $P_1 \geqslant P_2$. An isothermal profile is assumed for pressures above P_3 (Layer 3). Alternatively, for cooler atmospheres with no isothermal layer, Layer 2 could extend to deeper layers and Layer 3 could be absent (see Section 2.3).

have recently been determined to exist in several hot Jupiter atmospheres (Burrows et al. 2008). For the solar system giant planets, photochemical haze due to CH_4 is the primary cause of stratospheres, and for Earth it is O_3. For hot Jupiters, TiO and VO may be responsible for the thermal inversion (but see Spiegel et al. 2009), but the identification of the absorbers is still under debate. At still lower pressures, below $P \sim 10^{-5}$ bar, the optical depths eventually become so low that the layers of the atmosphere are transparent to the incoming and outgoing radiation.

2.2. A Parametric P–T Profile

We propose a parametric P–T profile, motivated by physical principles, solar system planet P–T profiles, and 1D "self-consistent" exoplanet P–T profiles generated from model atmosphere calculations reported in the literature. Our "synthetic" P–T profile encapsulates stratospheres, along with the low- and high-pressure regimes of the atmosphere. We will refer to our synthetic P–T profile as the "parametric P–T profile."

The atmospheric altitudes of interest are those where the spectrum is formed. Nominally, we consider this range to be between 10^{-5} bar $\leqslant P \leqslant 100$ bar, and we will refer to this pressure range as the "atmosphere" in the rest of the paper. At pressures lower than 10^{-5} bar, the atmosphere layers are nearly transparent to the incoming and outgoing radiation at visible and infrared wavelengths. And, above pressures of $\sim$100 bar (or even above pressures of $\sim$10 bar), the optical depth is too high for any radiation to escape without being reprocessed. The corresponding layers do not contribute significantly to the emergent spectrum. Figure 1 shows a schematic parametric P–T profile. In our model, we divide the atmosphere into three representative zones or "Layers" as shown in Figure 1. The upper-most layer, Layer 1, in our model profile is a "mesosphere" with no thermal inversions. The middle layer, Layer 2, represents the region where a thermal inversion (a "stratosphere") is possible. And, the bottom-most layer, Layer 3, is the regime where a high optical depth leads to an isothermal temperature structure. Layer 3 is used with hot Jupiters in mind; for cooler atmospheres this layer can be absent, with Layer 2 extending to deeper layers.

Our proposed model for the P–T structure in Layers 1 and 2 is a generalized exponential profile of the form

$$P = P_o e^{\alpha(T-T_o)^\beta}, \quad (1)$$

where, P is the pressure in bars, T is the temperature in K, and P_o, T_o, α, and β are free parameters. For Layer 3, the model profile is given by $T = T_3$, where T_3 is a free parameter.

Thus, our parametric P–T profile is given by

$$
\begin{aligned}
P_0 < P < P_1 &: P = P_0 e^{\alpha_1(T-T_0)^{\beta_1}} \text{ Layer1,} \\
P_1 < P < P_3 &: P = P_2 e^{\alpha_2(T-T_2)^{\beta_2}} \text{ Layer2,} \quad (2) \\
P > P_3 &: T = T_3 \text{ Layer3.}
\end{aligned}
$$

In this work, we empirically set $\beta_1 = \beta_2 = 0.5$ (see Section 2.3). The space of P–T profiles is spanned in all generality with the remaining parameters, rendering β redundant as a free parameter. Then, the model profile in Equation (2) has nine parameters, namely, P_0, T_0, α_1, P_1, P_2, T_2, α_2, P_3, and T_3. Two of the parameters can be eliminated based on the two constraints of continuity at the two layer boundaries, i.e., Layers 1–2 and Layers 2–3. And, in the present work, we set $P_0 = 10^{-5}$ bar, i.e., at the top of our model atmosphere. Thus, our parametric profile in its complete generality has six free parameters.

Our P–T profile consists of 100 layers in the pressure range of 10^{-5}–100 bar, encompassing the three zonal "Layers" described above. The 100 layers are uniformly spaced in $\log(P)$. For a given pressure, the temperature in that layer is determined from Equation (2), using the form $T = T(P)$. The kinks at the layer boundaries are removed by averaging the profile with a box-car of 10 layers in width.

2.3. Comparison with Known P–T Profiles

The parametric P–T profile described in Section 2.2 fits the actual temperature structures of a wide variety of planetary atmospheres. Figure 2 shows the comparison of our model P–T profile with published P–T profiles of several solar system planets and hot Jupiters. For each case, the published profile was fitted with our six-parameter P–T profile using a Levenberg–Marquardt fitting procedure (Levenberg 1944; Marquardt 1963). We were able to find best fits to all the published profiles with the β parameter fixed at 0.5, indicating that β is a redundant parameter. Therefore, we set $\beta_1 = \beta_2 = 0.5$ for all the P–T profiles in this work. In addition, it must be noted that, for the parametric P–T profile to have a thermal inversion, the condition $P_2 > P_1$ must be satisfied, and for one without a thermal inversion, $P_1 \geqslant P_2$.

For the solar system planets (top left panel of Figure 2), published profiles show detailed temperature structures obtained via several direct measurements and high-resolution temperature retrieval methods (Lindal et al. 1981, 1985, 1987, 1990; COESA 1976; http://atmos.nmsu.edu/planetary_datasets/). For hot Jupiters, on the other hand, observations are limited. Consequently, the published profiles for hot Jupiters (Figure 2) are obtained from self-consistent 1D models reported in the literature attempting to explain the available data on each system. As is evident from Figure 2, the parametric P–T profile provides good fits to all the known profiles. We emphasize that, while the fits alone are not a test of our retrieval method, they show that our parametric P–T profile is generally enough to fit the wide range of planetary atmospheres represented in Figure 2.

We also tested the emergent spectrum obtained with our parametric P–T profile by comparing it with a self-consistent
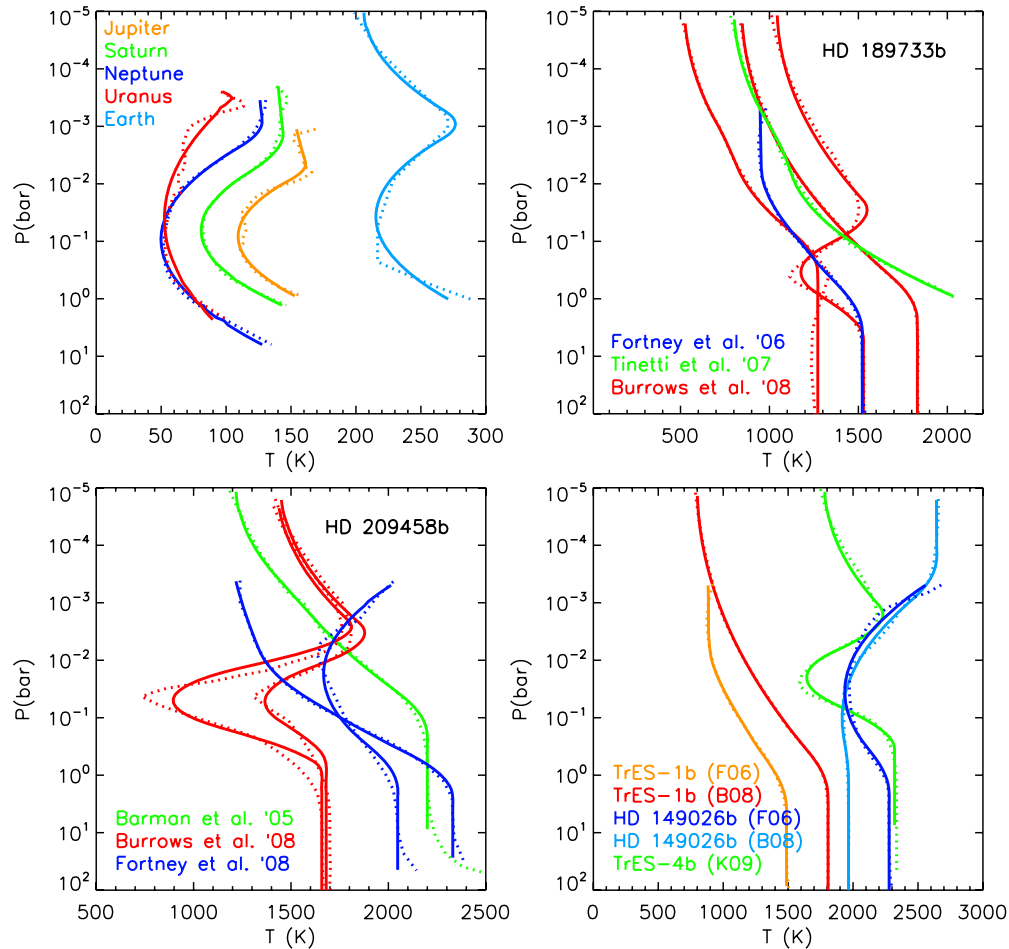
Figure 2. Comparison of the parametric *P–T* profile with previously published profiles. In each case, the dotted line is the published *P–T* profile and the solid line is a fit with the parametric profile (see Section 2.3). The *P–T* profiles of solar system planets (upper-left panel) were obtained from the NASA Planetary Data System (see the text for references). In the lower-right panel, "B08," "F06," and "K09" refer to Burrows et al. (2008), Fortney et al. (2006), and Knutson et al. (2009b), respectively.

model. In this regard, we used a *P–T* profile from a self-consistent atmosphere model (Seager et al. 2005) to generate an emergent spectrum for HD 209458b. The emergent spectrum calculated by our model (for the same molecular composition) agrees with that of the self-consistent model.

The fundamental significance of our parametric *P–T* profile is the ability to fit a disparate set of planetary atmosphere structures, with very different atmospheric conditions (Figure 2). In particular, the published hot Jupiter *P–T* profiles were obtained from several different modeling schemes. The different planetary atmospheres all conform to a basic mathematical model because of the common physics underlying the *P–T* profiles. We anticipate that our parametric *P–T* profile will open up a new avenue in retrieving *P–T* structure of exoplanetary atmospheres by enabling an efficient exploration of the temperature structures and compositions allowed by the data.

An important point concerns the adaptability of the model proposed in this work. The introduction of the isothermal Layer 3 in Equation (2) is motivated by the fact that hot Jupiters, which are the prime focus of this work, have convective–radiative boundaries that are deep in the atmosphere, and the presence of an isothermal Layer 3 is physically plausible (as is evident from self-consistent calculations in literature). However, the model can be adapted to cases of cooler atmospheres where the convective–radiative boundary occurs at lower pressures than for hot Jupiters, and where there may not be an isothermal

layer. The appropriate model *P–T* profile in such cases would be one with only the two upper layers (Layers 1 and 2). As can be seen from Figure 2, model fits to the solar system planets belong to the category of models with only Layers 1 and 2.

3. MODEL ATMOSPHERE

The goal of our model atmosphere is to be able to generate atmospheric spectra for a given planet over wide regions of parameter space and determine contours of fits with data. To meet this goal, our model uses efficient parameterization of the pressure–temperature structure and chemical composition of a planetary atmosphere. Our model atmosphere includes a 1D parametric *P–T* profile and parametric molecular abundances, coupled with line-by-line radiative transfer, hydrostatic equilibrium, and the requirement of energy balance at the top of the atmosphere. Given a set of parameter values, the output is the emergent spectrum, and a goodness-of-fit to a given data set.

The major difference of our model from traditional atmosphere models is in the treatment of energy balance. Our model requires energy balance at the top of the atmosphere, instead of an iterative scheme to ensure layer-by-layer radiative (or radiative + convective) equilibrium as is done in conventional models. For a given set of model parameter values, we require that the net energy output at the top of the atmosphere (obtained by integrating the emergent spectrum) balances the net energy

input due to the incident stellar flux (see Section 3.3). Models which do not satisfy this requirement are discarded. By running a large number of ($\sim 10^7$) models in the parameter space, and discarding those that do not satisfy the above requirement, we are left with a population of models that satisfy energy balance.

Our temperature and abundance retrieval method also differs from other retrieval methods (see Swain et al. 2008b, 2009a; Sing et al. 2008). Our work differs fundamentally by: using a parametric P–T profile, exploring a wide range in parameter space ($\sim 10^4$ P–T profiles independent of existing models, and $\sim 10^7$ models including abundances), maintaining hydrostatic equilibrium and global energy balance, and placing constraints on the day–night energy redistribution. We, therefore, consider our method to be a new step toward atmospheric temperature and abundance retrieval for extrasolar planets.

3.1. Radiative Transfer and Hydrostatic Equilibrium

We calculate emergent spectra using a 1D line-by-line radiative transfer code, assuming LTE. Our model atmosphere consists of 100 layers in the pressure range between 10^{-5} bar and 100 bar, and uniformly spaced in $\log(P)$. The key aspect of our model is the parameterization of the P–T profile and the chemical composition. In each layer, the parametric P–T profile (described in Section 2.2) determines the temperature and pressure. And, the density is given by the ideal gas equation of state. The radial distance is determined by the requirement of hydrostatic equilibrium. And, the equation of radiative transfer, assuming LTE and no scattering, is then solved along with the adopted molecular abundances (see Section 3.2 below) to determine the emergent flux. The geometry and the radiative transfer formulation are modified appropriately for calculating transmission spectra.

Our model directly computes the thermal emission spectrum and indirectly accounts for stellar heating and scattered radiation. In our model, we assume that the effects of heating by stellar radiation are included in the allowed "shapes" of the parametric P–T profile. As described in Section 2.3, our parametric P–T profile fits the P–T profiles obtained from self-consistent models that directly include absorbed stellar radiation, including profiles with thermal inversions.

One reason the approach of indirectly including stellar irradiation is valid is that the visible and infrared opacities are largely decoupled (Marley et al. 2002). For example, Na, K, TiO, VO can have strong absorption at visible wavelengths in brown dwarfs and exoplanets, yet are mostly negligible absorbers in the infrared. H_2O dominates infrared absorption, and CH_4 and CO are also spectroscopically active in the IR. Another reason the indirect account for stellar irradiation via a parametric P–T profile is justified is the uncertain chemistry (via unknown optical absorbers that in some cases cause thermal inversions) and physics that is hard to account for directly in a self-consistent 1D model. We note that it is not known whether the common assumption of radiative equilibrium in self-consistent models, while one possible way of including stellar irradiation, holds for hot Jupiter atmospheres.

We include molecules of hydrogen (H_2), water vapor (H_2O), carbon monoxide (CO), carbon dioxide (CO_2), methane (CH_4), and ammonia (NH_3). Our H_2O, CH_4, CO, and NH_3 molecular line data are from Freedman et al. (2008), and references therein. Our CO_2 data are from R. S. Freedman (2009, private communication) and Rothman et al. (2005). And, we obtain the H_2–H_2 collision-induced opacities from Borysow et al. (1997) and Borysow (2002).

3.2. Molecular Abundances

Molecular abundances in exoplanet atmospheres may depart from chemical equilibrium (Liang et al. 2003; Cooper & Showman 2006). Our code, therefore, has parametric prescriptions to allow for non-equilibrium quantities of each molecule considered. We begin by calculating a fiducial concentration of each molecule in a given layer, based on the assumption of chemical equilibrium. For chemical equilibrium we use the analytic expressions in Burrows & Sharp (1999), and assume solar abundances for the elements. The molecules we include are H_2O, CO, CH_4, CO_2, and NH_3. The molecule CO_2 is thought to originate from photochemistry and no simple expression for equilibrium composition is available; we therefore choose an arbitrary fiducial concentration. We denote the concentration of each molecule by its mixing ratio; i.e., number fraction with respect to molecular hydrogen.

The concentration of each molecule in a given layer is calculated by multiplying the corresponding fiducial concentration by a constant factor specific to each molecule. The constant factor corresponding to each molecule is a parameter of the model. Therefore, corresponding to the four prominent molecules, H_2O, CO, CH_4, and CO_2, in our model, we have four parameters: f_{H_2O}, f_{CO}, f_{CH_4}, and f_{CO_2}. For instance, f_{H_2O} is the ratio of the concentration of H_2O to the fiducial concentration of H_2O in each layer. Thus, although the concentration of H_2O is different in each layer, it maintains a constant ratio (f_{H_2O}) with the fiducial concentration in that layer. By varying over a range in these four parameters, we are essentially varying over a wide range of molecular mixing ratios and elemental abundances.

For NH_3, we restrict the concentration to the fiducial equilibrium concentration, i.e., $f_{NH_3} = 1$. This is because, NH_3 has limited and weak spectral features in the *Spitzer* and *HST* bands under consideration in this work. Additionally, NH_3 is not expected to be abundant in enhanced quantities at such high temperatures as are seen in hot Jupiters.

Clouds are not included in our model because HD 209458b and HD 189733b likely do not have clouds that scatter or emit at thermal infrared wavelengths. Several reasons have been proposed in literature justifying the use of cloud-free models for these planets: finding weak effects of clouds on the P–T profile (Fortney et al. 2006, 2008); fast sedimentation rates in radiative atmospheres (Barman et al. 2005); clouds forming too deep in the planetary atmosphere to affect the emergent spectrum (Fortney et al. 2006); spectral features in transmission dominated by molecular absorption over cloud particles (Showman et al. 2009, and references therein); haze absorption at blue wavelengths on HD 189733b drops off rapidly with increasing wavelength and should be negligible at IR wavelengths (Pont et al. 2008). That said, clouds can be included in our model as another free parameter, via a wavelength-dependent opacity, and we plan to make this extension in the future.

3.3. Energy Balance

A planetary atmosphere model must satisfy the fundamental constraint of energy conservation (here called energy balance). We consider a 1D plane-parallel atmosphere with normal incidence. While using a plane-parallel model, it is imperative to weight the incident stellar flux appropriately in order to represent an average dayside atmosphere.

The average stellar flux incident on the planetary dayside is given by $F_s = f F_\star$ where, $F_\star$ is the wavelength integrated stellar

flux at the substellar point of the planet. f is a geometric factor by which the stellar flux at the substellar point must be weighted so as to represent an average 1D plane-parallel incidence. A value of $f = \frac{1}{2}$ represents uniform distribution of stellar flux on the planet dayside; it comes from $F_\star \times (\pi R_p^2)/(2\pi R_p^2)$, i.e., the ratio of the planetary surface projected perpendicular to the incident stellar flux to the actual area of the planetary surface receiving the flux. However, it has been shown that just before secondary eclipse the dayside average flux should be biased toward a higher value of $f = \frac{2}{3}$ (Burrows et al. 2008). Therefore, in the present work, we adopt a value of $f = \frac{2}{3}$.

In the context of our 1D atmosphere, the constraint of energy balance means that the wavelength integrated emergent flux at the top of the planetary atmosphere matches the wavelength integrated incident stellar flux, after accounting for the Bond albedo (A_B) and possible redistribution of energy onto the night side (f_r). Our prescription for the day–night redistribution is similar to that of the P_n prescription of Burrows et al. (2006). We define f_r as the fraction of input stellar flux that is redistributed to the night side. The input stellar flux is given by $F_{in} = (1 - A_B)F_s$, i.e., the incident stellar flux (F_s), less the reflected flux ($A_B F_s$). Therefore, the energy advected to the night side is given by $f_r F_{in}$. And hence, the amount of flux absorbed on the dayside is given by $F_{in,day} = (1 - f_r)F_{in}$, which equals $(1 - A_B)(1 - f_r)F_s$. It is assumed that the intrinsic flux from the planet interior is negligible compared to the incident stellar irradiation.

Thus, the energy balance requirement on the dayside spectrum is given as

$$F_p = (1 - A_B)(1 - f_r)F_s, \qquad (3)$$

where, F_p is the wavelength integrated emergent flux calculated from the model spectrum. We use a Kurucz model for the stellar spectrum (Castelli & Kurucz 2004[3]). We adopt the stellar and planetary parameters from Torres et al. (2008).

We use energy balance, Equation (3), in two ways. The first, as described above, is to ensure that our model atmosphere satisfies energy conservation. The constraint on the model comes from the fact that A_B and f_r are bounded in the range [0, 1]. Thus, models for which $\eta = (1 - A_B)(1 - f_r)$ is greater than unity are discarded on grounds of energy balance. Second, for models which satisfy energy balance, Equation (3) gives us an estimate of η for a given model. If an A_B is assumed, this gives a constraint on f_r, and vice versa.

3.4. Parameter Space

The parameter space of our model consists of $N = N_{profile} + N_{molec}$ free parameters, where $N_{profile}$ is the number of parameters in the P–T profile, and N_{molec} is the number of parameters pertaining to the chemical composition. As described in Section 2, our parametric P–T profile has $N_{profile} = 6$, the six parameters being T_0, α_1, P_1, P_2, α_2, and P_3. And, corresponding to the four prominent molecules, H_2O, CO, CH_4, and CO_2, in our model, we have $N_{molec} = 4$ parameters: f_{H_2O}, f_{CO}, f_{CH_4}, and f_{CO_2} (see Section 3.2). Thus, our model has 10 free parameters.

Given a set of observations of a planet, for example, a dayside spectrum, our goal is to determine the regions of parameter space constrained by the data, and to identify the degeneracies therein. We investigate models with and without thermal inversions. To this effect, we run a large number of models on a grid

3 Also see ftp://ftp.stsci.edu/cdbs/grid/ck04models

in the parameter space of each scenario. Each parameter in either scenario has a finite range of values to explore, and we have empirically determined the appropriate step size in each parameter. A grid of reasonable resolution in this 10-parameter space can approach a grid-size that is computationally prohibitive.

Even before running the grid of models, however, the parameter space of allowed models can be constrained to some extent based on the data and energy balance. First, the model planet spectrum is bounded by two blackbody spectra, corresponding to the lowest and highest temperatures in the atmosphere. Correspondingly, the maximum and minimum temperatures, T_{max} and T_{min}, of the P–T profile are partly constrained by the maximum and minimum blackbody temperatures admissible by the data, and allowing a margin accounting for the fact that observations are available only at limited wavelengths. Second, an upper limit can be placed on the temperature at the base of our model atmosphere (T_3 in the P–T profile) based on energy balance. The maximum of T_3 is given by the effective temperature of the planet dayside assuming zero albedo and zero redistribution of the energy to the night side, and allowing for a factor close to unity ($\sim$1–1.5) to take into account the changes in the blackbody flux due to line features. Therefore, given the data, the space of P–T profiles can be constrained to some extent even before calculating the spectra, using the above conditions.

The final grid is decided by running several coarse grids, and obtaining an empirical understanding of the parameter space. At the end, a nominal grid in 10 parameters, with or without inversions in the P–T profiles, consists of $\sim$10^7 models. We thus computed a total of $\sim$10^7 models for each planet under consideration. We ran the models on $\sim$100 2 GHz processors on a Beowulf cluster, at the MIT Kavli Institute for Astrophysics and Space Research, Cambridge, MA.

3.5. Quantitative Measure of Error

Broadband observations of exoplanet atmospheres are currently limited to the six channels of broadband infrared photometry using *Spitzer*. Additionally, a few narrowband spectrophotometry have also been reported using the *HST* NICMOS G206 grism (1.4–2.6 μm), and the *Spitzer* IRS spectrograph (5–14 μm). The number of broadband observations available in a single data set are typically smaller than the number of parameters in our model. Also, given that the parameters in our model are highly correlated and the degeneracies not well understood, the nature of existing data does not allow spectral fitting in the formal sense.

Consequently, our approach in this work is to compute a large number of models on a pre-defined grid in the parameter space. For each model, we calculate a "goodness-of-fit" with the data using a statistic defined by a weighted mean squared error, given by

$$\xi^2 = \frac{1}{N_{obs}} \sum_{i=1}^{N_{obs}} \left(\frac{f_{i,model} - f_{i,obs}}{\sigma_{i,obs}} \right)^2. \qquad (4)$$

Here, f_i is the flux observable and N_{obs} is the number of observed data points. $f_{i,obs}$ and $f_{i,model}$ are the observed f_i and the corresponding model f_i, respectively. For secondary eclipse spectra, f_i is the planet-star flux contrast, whereas, for transmission spectra, f_i is the transmission. $\sigma_{i,obs}$ is the 1σ measurement uncertainty in the observation. In order to obtain the model fluxes in the same wavelength bins as the observation,

we integrate the model spectra with the transmission functions of the instruments. Where spectrophotometry is available, we additionally convolve our model spectra with the instrument point-spread function.

The goodness-of-fit (ξ^2), as defined in Equation (4), is similar in formulation to the conventional definition of the reduced χ^2 statistic, if N_{obs} is replaced by the number of degrees of freedom. In the current context, we refrain from using the χ^2 statistic to asses our model fits because our number of model parameters (N) are typically more than the number of available broadband data points, leading to negative degrees of freedom. A value of χ^2 with negative degrees of freedom lacks meaning in that we cannot relate it to a confidence level. Therefore, in using ξ^2 as our statistic of choice, we are essentially calculating χ^2 per data point as opposed to χ^2 per degree of freedom. We discuss this further in Section 6.2.

4. RESULTS: HD 189733B

4.1. Secondary Eclipse

HD 189733b has the best data set for any hot Jupiter known to date, including both signal-to-noise and wavelength coverage. Several remarkable observations of the planet dayside have been made by determining the planet-star flux ratios just before secondary eclipse. Grillmair et al. (2008) reported an infrared spectrum of the dayside in the 5–14 μm range, obtained with the *Spitzer* IRS instrument. Charbonneau et al. (2008) presented broadband photometry in the six *Spitzer* channels (3.6, 4.5, 5.8, 8, 16, and 24 μm).[4] Separate photometric observations in the *Spitzer* 8 μm and 24 μm channels were also reported by Knutson et al. (2007, 2009a), respectively. Additionally, an upper limit was placed on the 2.2 μm flux contrast by Barnes et al. (2007). More recently, Swain et al. (2009a) observed the planet dayside with *HST* NICMOS spectrophotometry in the 1.5–2.5 μm range.

Together, these data sets place important constraints on the dayside atmosphere of the planet. The high signal-to-noise ratio (S/N) IRS spectrum reported by Grillmair et al. (2008), obtained with 120 hr of integration time, is the best exoplanet spectrum known. This spectrum forms the primary data set for our present study of HD 189733b. In addition, we also use the photometric observations of Charbonneau et al. (2008), and the spectrophotometric observations of Swain et al. (2009a) to place complementary constraints.[5] We use the two independent observations of Knutson et al. (2007, 2009a), at 8 μm and 24 μm, only as a guide for the models, and exclude them from our fits. This is because we place constraints from each individual data set separately, for reasons explained below, and we cannot place any constraints from a single data point from each of Knutson et al. (2007, 2009a). However, it must be noted that the 8 μm and 24 μm values of Knutson et al. (2007, 2009a) agree with the IRS spectrum and the Charbonneau et al. (2008) observations, respectively, which are being used in the current work. We present the data in Figure 3, along with model fits.

We analyze each data set separately. The reason we use a separate treatment is that some individual observations at similar wavelengths differ from each other. Specifically, the 8 μm *Spitzer* Infrared Array Camera (IRAC) data point from

---

[4] The 16 μm value of Charbonneau et al. (2008) was obtained by reanalyzing the observations of Deming et al. (2006), and has been found to be consistent with the latter.

[5] We do not use those binned data points of Swain et al. (2009b) that are either at the edges of the chip or are non-detections at the 3σ level. These include points with $\lambda < 1.65$ μm and $\lambda > 2.4$ μm.
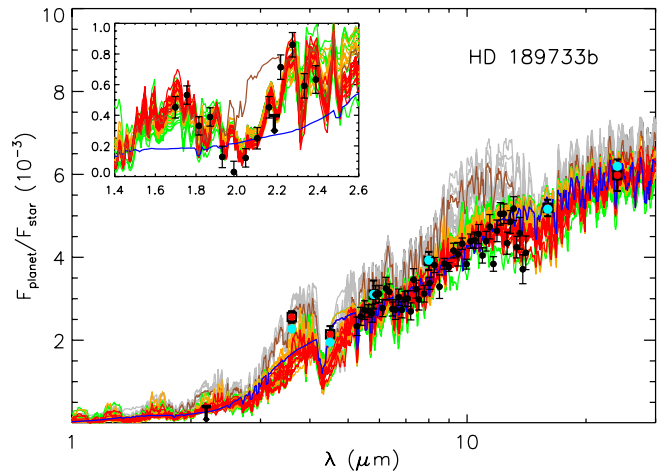

Figure 3. Secondary eclipse spectra for HD 189733b. The black squares (filled with red) with error bars show the data from *Spitzer* photometry in six channels, at 3.6, 4.5, 5.8, 8, 16, and 24 μm, reported by Charbonneau et al. (2008; the 16 μm point is from reanalysis of Deming et al. 2006, consistent with the latter). The black circles with error bars show the IRS data from Grillmair et al. (2008), and those in the inset show the *HST* NICMOS data from Swain et al. (2009b; see Section 4.1 for details). The upper limit at 2.2 μm shows the 1σ constraint from Barnes et al. (2007). In the main panel, the red, orange, and green spectra show model spectra that fit the IRS spectrum with ξ^2 in the range of 1.0–2.0, 2.0–3.0, and 3.0–4.0, respectively. Ten spectra from each category are shown. For guidance, a single best-fit model spectrum for this data is shown in blue. The gray spectra in the main panel show 10 of the models that fit the *Spitzer* broadband photometry with $\xi^2 \leqslant 2.0$. For guidance, a single best-fit model spectrum for this data is shown in brown (with the bandpass averaged points shown in light blue). The inset shows 10 of the model spectra that fit the NICMOS data; with colors following those in the main panel. The blue and brown models in the inset are one each best-fit to the IRS data and photometric data, respectively, showing that the best-fit models for the IRS data and the broadband photometry do not match the NICMOS data.

Charbonneau et al. (2008) is $\sim$2σ above the IRS spectrum at the same wavelength (Grillmair et al. 2008). Also, 8 μm IRAC observations taken at separate times differ by over 2σ (Charbonneau et al. 2008). From a model interpretation viewpoint, a 2σ spread means that almost no constraints on molecular abundances can be drawn (based on the reported uncertainties in the data). In addition, the very strong evidence of CO_2 that is visibly obvious around 2 μm in the *HST*/NICMOS data set is not so strong in the 4.5 μm and 16 μm *Spitzer* channels. In this work, we are unable to find models that fit all the three data sets of HD 189733b simultaneously within the $\xi^2 = 2$ level. The data and model results below may well indicate atmospheric variability in this planet. See Section 6.3 for further discussion about possible atmospheric variability.

In what follows, we describe the constraints on the atmospheric properties of HD 189733b placed by each data set. Ideally, we would like to report constraints at the $\xi^2 = 1$ surface, i.e., only those models which, on an average, fit the observations to within the 1σ error bars. However, we adopt a more conservative approach and lay emphasis on the results at the $\xi^2 = 2$ surface as well, allowing for models fitting the observations to within $\sim 1.4\sigma$ on an average. The latter choice is somewhat arbitrary, and the informed reader could choose to consider other ξ^2 surfaces; we show contours of ξ^2 in the different atmospheric properties.

4.1.1. Molecular Abundances

The constraints on the abundances due to the different data sets are shown in Figure 4. The figure shows contours of ξ^2 in the parameter space of our model atmosphere. The contours
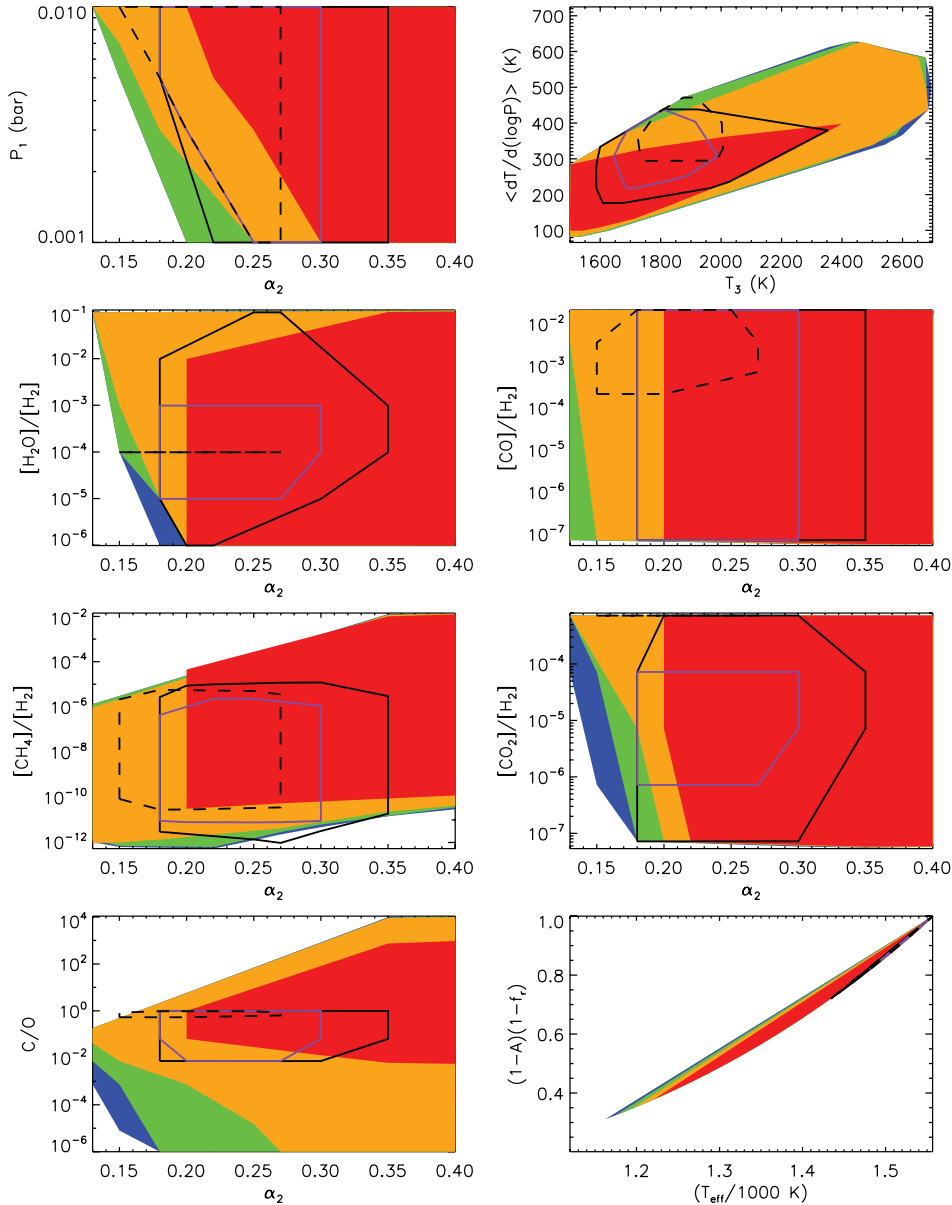
Figure 4. Constraints on the dayside atmosphere of HD 189733b. The contours show minimum ξ^2 surfaces in the parameter space; at each point in a two-parameter space, the color shows the minimum possible ξ^2 out of a degenerate set of solutions (see Section 4.1.1 for details). The filled color surfaces show the constraints due to the *Spitzer* IRS spectrum (Grillmair et al. 2008). The red, orange, green, and blue colors correspond to ξ^2 ranges of 1.0–2.0, 2.0–3.0, 3.0–4.0, and 4.0–5.0, respectively. The solid lines show the constraints from *Spitzer* broadband photometry (Charbonneau et al. 2008); the black (purple) solid lines correspond to the $\xi^2 < 2$ ($\xi^2 < 1$) surface. The dashed lines show the $\xi^2 < 2$ constraints from *HST* NICMOS Spectrophotometry (Swain et al. 2009b). The results follow from $\sim 9 \times 10^6$ models. The mixing ratios of species are shown as ratios by number. $< dT/d(\log P) >$ is the average temperature gradient in Layer 2 of the *P–T* profile, which contributes most to the emergent spectrum.

show minimum ξ^2 surfaces. At each point in a given two-parameter space, several values of ξ^2 are possible because of degeneracies with other parameters in the parameter space. In other words, the same point in a pair of parameters can have multiple values of ξ^2 corresponding to evaluations at various values in the remaining parameters. For the contours in Figure 4, we consider the minimum possible value of ξ^2 at each point in a two-parameter space. Consequently, each colored surface shows the region of parameter space which allows a minimum possible ξ^2 corresponding to that color. The mixing ratios of species are shown as ratios by number.

Spitzer IRS spectrum. We begin with the IRS spectrum (Grillmair et al. 2008) because this data set has the broadest wavelength coverage and the best S/N. Also, the IRS data set has more data points than the number of parameters in our model.

Our most significant new finding is the existence of models fitting the IRS data set that are totally consistent with efficient redistribution of energy from the planet dayside to the night side (see Figure 4 for the range of allowed values). This addresses a significant problem in previously published models for dayside spectra (Grillmair et al. 2008) not being able to explain the efficient redistribution found in the phase curves of Knutson et al. (2007, 2009a; see Charbonneau et al. 2008 and Grillmair et al. 2008; but also see Barman 2008). With the IRS data, we also confirm the absence of a thermal inversion in HD 189733b.

Despite the high S/N, the IRS spectrum allows only weak constraints on the molecular abundances. The reason being that the IRS spectral range has molecular absorption features of only CH_4 and H_2O; even for these molecules, their features at other wavelengths remain completely unconstrained. The significant

features are of CH_4 (7.6 μm), and H_2O (6.3 μm). For example, the $\xi^2 = 2$ surface constrains the mixing ratio of water vapor to 10^{-6}–0.1, and that of CH_4 to be less than 10^{-2} (but cf. Section 6.4).

Spitzer broadband photometry. Our model fits to the *Spitzer* broadband data (Charbonneau et al. 2008) require less efficient circulation of incident stellar energy compared to the best model fits to the *Spitzer* IRS spectrum. Specifically, the value for redistribution in our framework is $f_r \lesssim 0.25$, and this agrees with previous results (Barman 2008; Charbonneau et al. 2008) which find that model fits to the broadband data require inefficient day–night redistribution of energy. The discrepancy in redistribution arises from different planet-star contrast ratios. The 8 μm IRAC point of Charbonneau et al. (2008) is $\gtrsim 2\sigma$ different from the IRS spectrum, and from the 8 μm IRAC measurement of Knutson et al. (2007). Similar to the IRS spectrum, the *Spitzer* broadband photometry shows no sign of a thermal inversion.

The *Spitzer* broadband photometry enables significant constraints on molecular abundances. Again, we take the $\xi^2 = 2$ surface, corresponding to an average difference of 1.4σ between the model and data. We find the lower limit of the H_2O mixing ratio to be 10^{-6}, and the upper limit of the CH_4 mixing ratio to be 10^{-5} (Figure 4). At the $\xi^2 = 2$ surface there are no constraints on the presence or abundances of CO and CO_2. At the $\xi^2 = 1$ surface, the best-fit models constrain the molecular mixing ratios as follows: $10^{-5} \leqslant H_2O \leqslant 10^{-3}$; $CH_4 \leqslant 2 \times 10^{-6}$; $7 \times 10^{-7} \leqslant CO_2 \leqslant 7 \times 10^{-5}$; CO is unconstrained because it is degenerate with CO_2. The identification of CO_2, at the $\xi^2 = 1$ surface, is intriguing, and this is the first time CO_2 is identified with *Spitzer* photometry. Our model also finds the C/O ratio to be $7 \times 10^{-3} \leqslant C/O \leqslant 1$ for both the $\xi^2 = 1$ and $\xi^2 = 2$ surfaces.

HST/NICMOS spectrophotometry. The *HST*/NICMOS data (Swain et al. 2009a) are useful because the wavelength range includes significant features of H_2O, CH_4, CO, and CO_2 (Figure 3). We can therefore constrain the abundances even at the $\xi^2 = 2$ surface (Figure 4). We find mixing ratios of: H_2O $\sim 10^{-4}$; $CH_4 \leqslant 6 \times 10^{-6}$; $2 \times 10^{-4} \leqslant CO \leqslant 2 \times 10^{-2}$; and $CO_2 \sim 7 \times 10^{-4}$. It is remarkable that at the $\xi^2 = 2$ surface we can constrain the abundances so stringently. The exception is CH_4, where the upper limit indicates that methane is not present in large quantities on the dayside of HD 189733b. The C/O ratio is between 0.5 and 1. Our inferred abundances are consistent with those reported in Swain et al. (2009a), with the major exception of CO_2. While we find CO_2 mixing ratios of 7×10^{-4}, Swain et al. (2009a) find $10^{-7} \leqslant CO_2 \leqslant 10^{-6}$. At present we have no explanation for this discrepancy.

A mixing ratio of 7×10^{-4} is seemingly high from a theoretical standpoint; photochemistry which is thought to be the primary source of CO_2 in hot Jupiters allows mixing ratios of CO_2 up to $\sim 10^{-6}$, assuming solar metallicities (Liang et al. 2003; Zahnle et al. 2009). One possible explanation of a large inferred CO_2 mixing might be a high mixing ratio concentrated in only a few layers of the atmosphere. The data can be fit equally well with the same mixing ratio (7×10^{-4}) of CO_2 present only between 10^{-3} and 0.3 bar causing an average mixing ratio of 10^{-6} over the entire atmosphere.

4.1.2. Pressure–Temperature Profiles

Our results include constraints on the 1D averaged *P–T* profile. We explore the parameter space with a grid of $\sim 10^4$
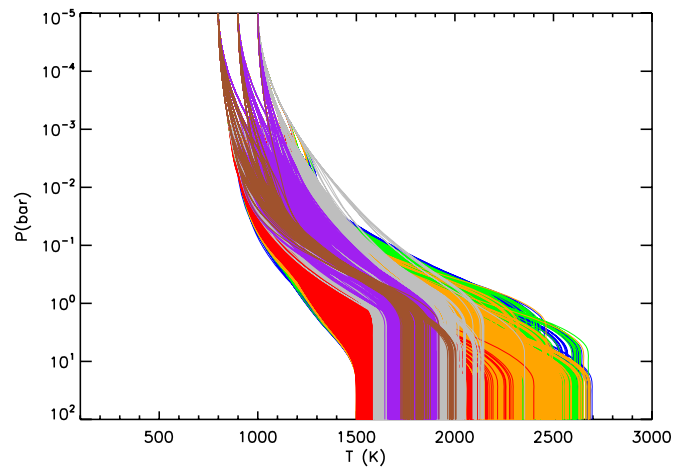

Figure 5. Pressure–temperature profiles explored by models for the secondary eclipse spectrum of HD 189733b. Since each *P–T* profile can have multiple values of ξ^2, corresponding to the several possible molecular compositions, we color-code each *P–T* profile with only the minimum possible value of ξ^2 (as also described in Figure 4). The red, orange, green, and blue colors correspond to models that fit the IRS spectrum (Grillmair et al. 2008) with minimum ξ^2 in the ranges of 1.0–2.0, 2.0–3.0, 3.0–4.0, and 4.0–5.0, respectively. The purple and gray profiles correspond to models that fit the *Spitzer* broadband photometry (Charbonneau et al. 2008) with minimum ξ^2 in the ranges 0.0–1.0 and 1.0–2.0, respectively, and the brown profiles show models that fit the NICMOS data (Swain et al. 2009b) with the minimum ξ^2 in the 1.0–2.0 range.

P–T profiles, shown in Figure 5. For *P–T* profiles with no thermal inversions, the parameters that influence the spectrum most are the two pressures (P_1 and P_3), which contribute the temperature differential in Layer 2 of the atmosphere, and the corresponding slope (α_2). Additionally, P_3 governs the base flux, corresponding to the blackbody flux of temperature T_3, on which the absorption features are imprinted.

The constraints on the parameters of the *P–T* profiles (Section 2.2) from the three data sets are shown in Figure 4. The IRS spectrum (Grillmair et al. 2008) constrains the *P–T* profiles toward larger values of α_2, leading to less steep temperature gradients. For the same base temperature (T_3) of the planet dayside, the maximum temperature gradients allowed by the broadband photometry and the *HST* spectrum are always higher than that allowed by the IRS data set. The $\xi^2 = 2$ surface for the IRS data set constrains α_2 to be greater than 0.2, while the constraints due to the broadband photometry and the *HST* data are 0.18–0.35 and 0.15–0.27, respectively. The same surface constrains the mean temperature gradient ($< dT/d \log P >$) in Layer 2 to 100–400 K, 180–440 K, and 290–470 K for the IRS, the broadband photometry, and the *HST* data sets, respectively. The $\xi^2 = 2$ surface also shows that the IRS data allow for lower base temperatures as compared to the other data sets. The skin temperature (T_0) at the top of the atmosphere (at $P \sim 10^{-5}$ bar) is relatively unconstrained because of its degeneracy with the temperature gradient, and because of the low contribution of spectral features at that pressure.

4.1.3. Albedo and Energy Redistribution

Our results also constrain the albedo and day–night energy redistribution. The relevant parameter is $\eta = (1 - A_B)(1 - f_r)$, where A_B is the Bond albedo, and f_r is the fraction of input stellar flux redistributed to the night side (see Section 3.3). Since we can only constrain the product η and not the individual components, A_B and f_r, one can estimate the constraint on A_B given f_r or vice versa. This is similar to other forward models in the literature,

where an f_r is assumed, and the albedo is determined by the model. Figure 4 shows the ξ^2 surface in the space of T_{eff} versus η. The IRS data set allows for efficient day–night circulation on this planet, with η in the range 0.38–0.99 at the $\xi^2 = 2$ level. While $\eta = 1$ means zero albedo and no redistribution, a value of $\eta = 0.38$ translates into an upper limit of $f_r \leqslant 0.62$ (for zero albedo). Even if one were to assume $A_B = 0.3$ (a relatively high value for hot Jupiters; see Rowe et al. 2008), f_r can be as high as 0.46, indicating very efficient redistribution. The broadband photometry and the *HST* data sets, on the other hand, require much lower efficiency in energy redistribution, constraining the lower bound on η, at the $\xi^2 = 2$ level, to values of 0.74 and 0.72, respectively. These values translate into upper limits on f_r of 0.26 and 0.28, respectively, suggesting low redistribution. The range of effective temperatures allowed by the different data sets follow accordingly. While the IRS data set allows for T_{eff} between 1220 and 1550 K, the broadband photometry and *HST* data sets constrain T_{eff} between 1440 and 1560 K.

It is natural to ask: what can we say with the combined data sets from *Spitzer* IRS, *Spitzer* IRAC, and *HST* NICMOS? The answer depends on which error surface one is willing to adopt. Each of the data sets places a different constraint on the planet atmosphere (at the $\xi^2 \leqslant 2$ surface). Thus, if we take the data sets at face value, and adopt the model $\xi^2 \leqslant 2$ surfaces, we find that the atmosphere must be variable, both in its energy redistribution state and in the chemical abundances. Specifically, the high CO_2 value could be pointing to local changes due to transient photochemical effects and atmospheric flows. On the other hand, inference of stellar variability, or refined observational uncertainties may potentially change this situation.

4.2. Transmission Spectra

The transmission spectrum of HD189733b was presented by Swain et al. (2008b), who reported the detection of CH_4 and H_2O in the 1.4–2.5 μm range covered by the *HST*/NICMOS spectrophotometry. Transmission data are complementary to secondary eclipse data, because a transmission spectrum probes the part of the planet atmosphere in the vicinity of the limb, whereas secondary eclipse data probe the planetary dayside. In addition, a transmission spectrum reveals line features of the species in absorption, imprinted on the stellar flux, with the self-emission of the planet contributing negligibly to the observed flux.

We computed $\sim 7 \times 10^5$ models to place constraints on allowed limb P–T profiles and quantify the allowed abundances by the ξ^2 surfaces. In order to compute the ξ^2, our models were convolved with the instrument point-spread function, integrated over the grism transmission function, and finally binned to the same bins as the data (as described in Swain et al. 2008b). We find that 2 of 18 binned data points (at 1.888 μm and 2.175 μm) as reported by Swain et al. (2008b) have unusually high values, and amount to an unusually large contribution to the net ξ^2. In the framework of our models, we do not find any spectral features that might be able to explain those values. Consequently, we leave these two points out of our present analysis. Figure 6 shows the model spectra and data.

4.2.1. Molecular Abundances

Our results confirm the presence of H_2O and CH_4 in the limb, as also reported by Swain et al. (2008b). At the $\xi^2 = 2$ surface, as shown in Figure 7, the H_2O mixing ratio is constrained to 5×10^{-4}–0.1, and the CH_4 mixing ratio lies between 10^{-5} and 0.3. These ranges of mixing ratios for H_2O and CH_4 are
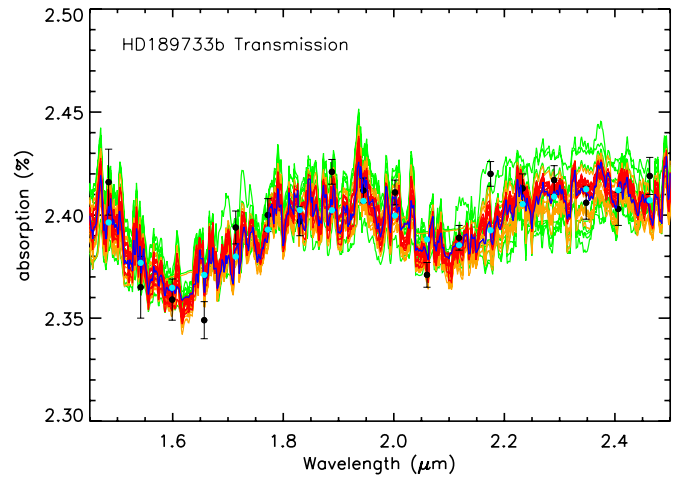

Figure 6. Transmission spectra for HD 189733b. The black filled circles with error bars show the data from Swain et al. (2008b; see Section 4.2 for details). The red, orange, and green spectra show 10 models each in the ξ^2 ranges of 1.0–2.0, 2.0–3.0, and 3.0–4.0, respectively. The blue spectrum shows one best-fit model, with the light-blue filled circles showing the corresponding model points binned to the grism bandpass, after convolving with the instrument point-spread function as described in Swain et al. (2008b).

consistent with the mixing ratios found for the best-fit model reported by Swain et al. (2008b). Although, these constraints are roughly consistent with the constraints on the same molecules on the dayside inferred in Section 4.1, the high mixing ratios of CH_4 allowed is appalling at first glance. This hints at a region of high CH_4 concentration in the limb, possibly on the night side. The effect of other possible molecules, CO, NH_3, and CO_2 on the spectrum is minimal. Although each of these molecules have some spectral features in the observed wavelength range, the upper limits on their compositions placed by the data are not statistically significant.

4.2.2. Pressure–Temperature Profiles

Figure 8 shows the P–T profiles explored for the HD 189733b transmission data set. The best-fit models with $\xi^2 \leqslant 2$ are shown in red. Figure 7 shows the ξ^2 surface in the parameters space of the P–T profiles. The best-fit models are consistent with an atmosphere with no thermal inversions. The α_2 parameter is constrained by the $\xi^2 = 2$ surface to be greater than ~ 0.15, and the temperature T_3 at the limb is constrained to lie between 1500 K and 2250 K. The mean temperature gradient ($< dT/d \log P >$) in Layer 2 constrained by the $\xi^2 = 2$ surface lies between 130 K and 550 K.

5. HD 209458B RESULTS: SECONDARY ECLIPSE

The dayside of HD 209458b has been of substantial interest, owing to the indication of a thermal inversion in the atmosphere of this planet. Deming et al. (2005) reported the first detection of thermal emission from HD 209458b in the 24 μm Multiband Imaging Photometer (MIPS) Channel of *Spitzer*. Knutson et al. (2008) reported broadband photometry of the planet-star flux ratio in the four *Spitzer* IRAC channels (3.5, 4.6, 5.8, 8 μm). Newer photometric observations have been made by Deming in the 16 μm IRS Channel and, an updated value is available for the 24 μm MIPS Channel (D. Deming 2009, private communication). Richardson et al. (2003) observed an upper limit on the contrast ratio in the K band (2.2 μm) using IRTF SpeX. Additionally, Richardson et al. (2007) and Swain et al.
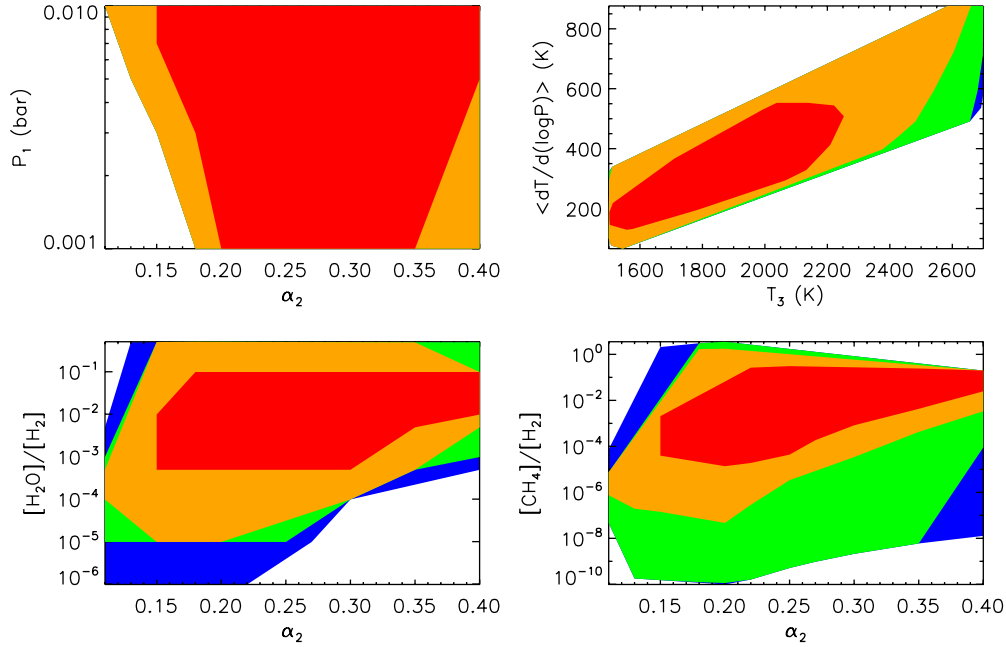
Figure 7. Constraints on atmospheric properties at the limb of HD 189733b. The contours show minimum ξ^2 surfaces (see caption of Figure 4 for details), as constrained by the transmission spectrum of Swain et al. (2008b) described in Section 4.2. The red, orange, green and blue surfaces correspond to ξ^2 in the ranges 1.0–2.0, 2.0–3.0, 3.0–4.0, and 4.0–5.0, respectively.
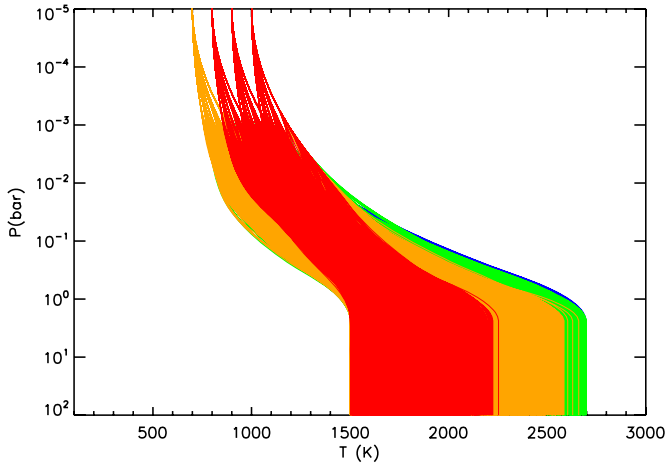

Figure 8. Pressure–temperature profiles explored by models for the transmission spectrum of HD 189733b. The profiles are color-coded by minimum ξ^2 (see Figure 5), and the colors are described in Figure 7.
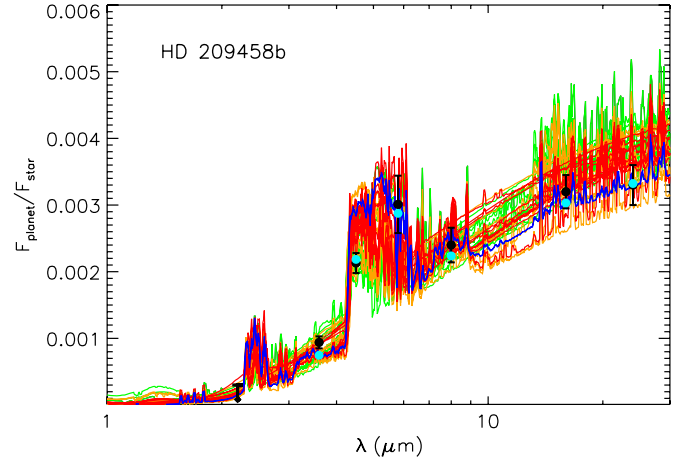

Figure 9. Secondary eclipse spectra for HD 209458b. The black filled circles with error bars show the data, obtained by *Spitzer* photometry. The 3.6 μm, 4.5 μm, 5.8 μm, and 8 μm data are from Knutson et al. (2008). The 16 μm and 24 μm data are from D. Deming (2009, private communication). The upper limit at 2.2 μm shows the 1σ constraint from Richardson et al. (2003). The red, orange, and green spectra correspond to models with ξ^2 in the range of 0.0–2.0, 2.0–3.0, and 3.0–4.0, respectively. For guidance, a single best-fit model spectrum is shown in blue (with the bandpass averaged points shown in light blue).

(2008a) presented a low S/N *Spitzer* IRS spectrum in the 7.5–13.2 μm range. And, after submitting our present work, we became aware of an independent inference of H_2O, CH_4, and CO_2 in HD 209458b, based on *HST* NICMOS observations, and five-channel *Spitzer* photometry; although, a quantitative measure of fit was not reported (Swain et al. 2009b). Here, we report independent detections of H_2O, CH_4, CO_2, and CO based on quantitative constraints at the $\xi^2 < 1$ level of model fits to six-channel *Spitzer* photometry.

For HD 209458, we compute model fits to the six *Spitzer* broadband photometric detections (at 3.6, 4.5, 5.8, 8, 16, and 24 μm), combining data from Knutson et al. (2008) and D. Deming (2009, private communication). We do not use the IRS spectrum (Richardson et al. 2007; Swain et al. 2008b) because the S/N is too low to yield significant model constraints.

We explore a grid of 6×10^6 models for this system. Figure 9 shows sample model spectra and the data for the planet-star

flux contrast in this system. The figure shows model spectra at different levels of ξ^2. As shown in the figure, our best-fit spectra (a sample binned spectrum is shown in light blue) fit all the available data to within the 1σ error bars. And, our $\xi^2 = 2$ models match the observations to $\sim 1.4\sigma$ on average.

5.1. Molecular Abundances

Our results indicate the presence of H_2O, CO, CH_4, and CO_2 in the atmosphere of HD 209458b. As will be discussed in Section 5.2, the allowed *P–T* profiles show the existence of a deep thermal inversion in the atmosphere of HD 209458b. Consequently, all the line features of the molecules are seen as
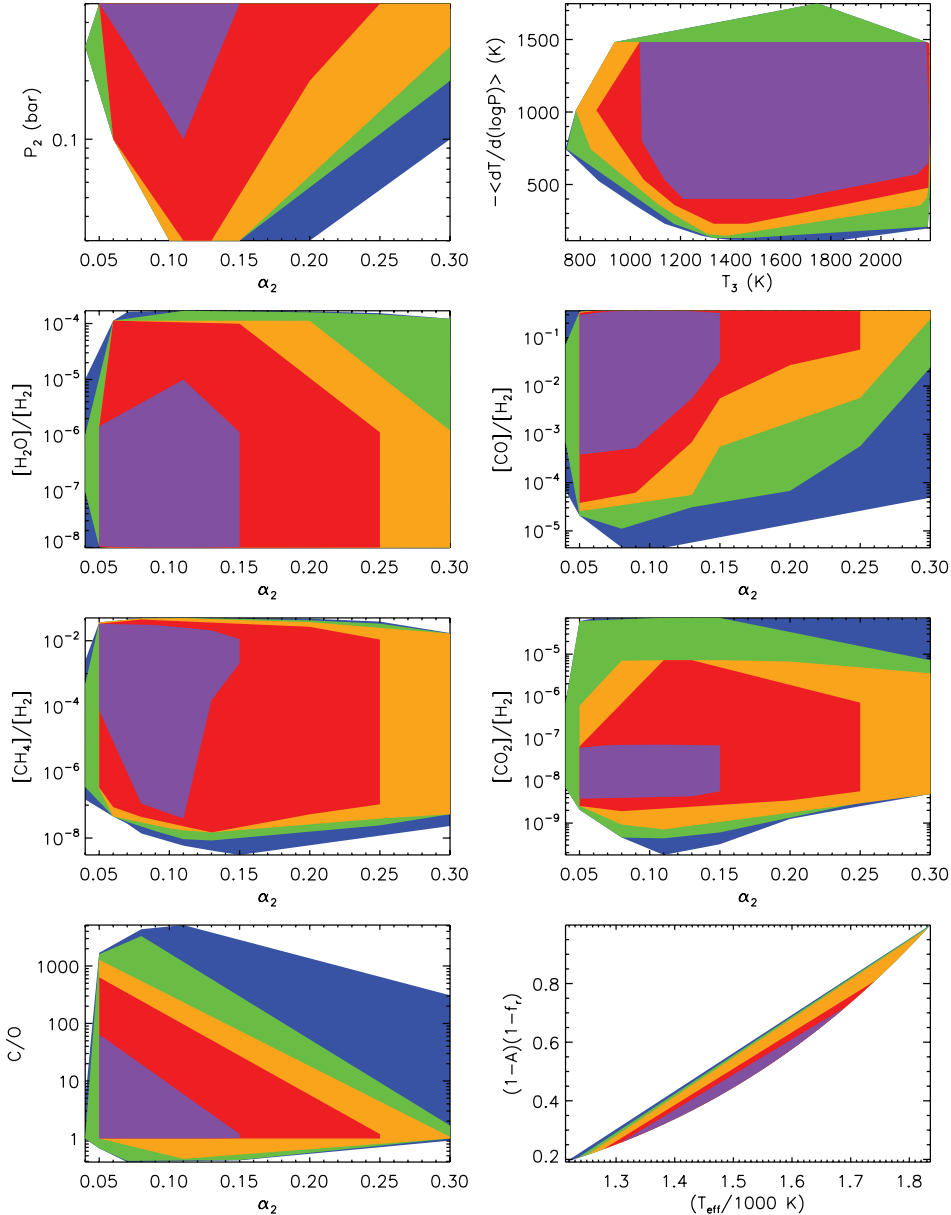
Figure 10. Constraints on the dayside atmosphere of HD 209458b. The contours show minimum ξ^2 surfaces (see Figure 4) in the parameter space of models for secondary eclipse spectra of HD 209458b. The red, orange, green, and blue surfaces correspond to ξ^2 in the ranges 1.0–2.0, 2.0–3.0, 3.0–4.0, and 4.0–5.0, respectively. Additionally, the purple colored surfaces show regions that allow $\xi^2 < 1$. The results follow from $\sim 6 \times 10^6$ models with thermal inversions. Models without thermal inversions are ruled out by the data. $< dT/d(\log P) >$ is the average temperature gradient in the atmosphere between pressures P_1 and P_2, in P–T profiles with thermal inversions, which contributes most to the observed emission features.

emission features, rather than absorption features as in the case of HD 189733b. The constraints on the concentrations of all the molecules are shown in Figure 10.

The $\xi^2 = 2$ surface places an upper limit on the mixing ratio of H_2O at 10^{-4}, with the $\xi^2 = 1$ surface allowing mixing ratios up to 10^{-5}. The limits on H_2O are governed by the band features of the molecule in the 5.8 μm and 24 μm channels. While the upper limit on the mixing ratio of H_2O is well constrained, the constraint on the lower limit is rather weak, allowing values as low as 10^{-8} at $\xi^2 = 1$. The stringent upper limit on H_2O comes primarily from the low planet-star flux contrast observed in the 24 μm channel. Similarly, the high flux contrast observed in the 5.8 μm channel should, in principle, yield a stringent lower limit. However, the weak lower limit is because of the large observational uncertainty on the flux contrast in the 5.8 μm

channel. The 1σ error bar on the observed 5.8 μm flux contrast is the largest of uncertainties in all the channels, and 1.5 times larger than the error bar on the 24 μm flux contrast.

The $\xi^2 = 2$ constraint on the mixing ratio of CH_4 is 10^{-8}–0.04, based on band features in the 3.6 μm and 8 μm channels. Although the features in the 3.6 μm channel are degenerate with some features of H_2O in the same channel, the exclusive CH_4 features in the 8 μm channel break the degeneracy. The $\xi^2 = 2$ surface places an absolute lower limit on CO at 4×10^{-5}, and requires a mixing ratio of CO_2 between 2×10^{-9} and 7×10^{-6}. The need for CO_2 arises from the high contrast observed between the 4.5 μm and the 3.6 μm channels. The 4.5 μm channel could in principle be explained by CO alone. However, such a proposition would require large amounts of CO, close to mixing ratios of 1. CO_2 provides additional absorption in the
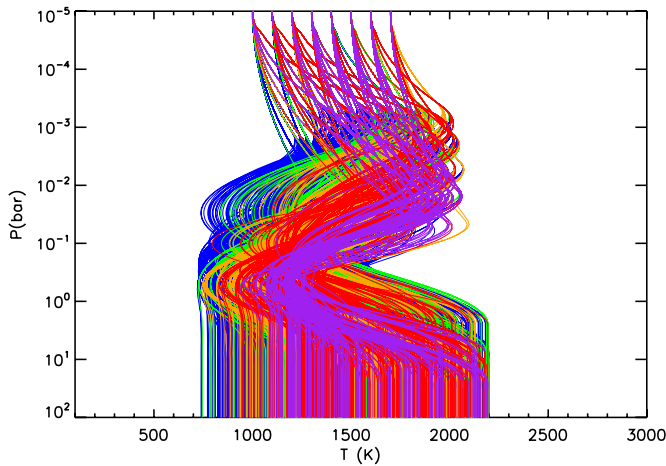
Figure 11. Pressure–temperature profiles explored by models for the secondary eclipse spectrum of HD 209458b. All the profiles have an inversion layer. Profiles without thermal inversions are ruled out by the data. The profiles are color-coded by minimum ξ^2 (as described in Figure 5), and the colors are described in Figure 10.

same 4.5 μm channel, with a relatively reasonable abundance. In addition, the amount of CO_2 is also constrained by the 16 μm channel—too high of a CO_2 abundance would not agree with the data because CO_2 has a strong absorption feature in the 16 μm channel. Thus, the 4.5 μm and 16 μm channels together constrain the amounts of CO_2, thereby also constraining the CO feature in the 4.5 μm channel. If the 16 μm data did not exist, there would have been a large degeneracy in the abundances of CO and CO_2.

If we consider the $\xi^2 = 1$ surface, instead of the $\xi^2 = 2$ surface, our results place tighter constraints on all the molecules. At this surface, the constraints on the mixing ratios are: $10^{-8} \leqslant$ $H_2O \leqslant 10^{-5}$; $4 \times 10^{-8} \leqslant CH_4 \leqslant 0.03$; $CO \geqslant 4 \times 10^{-4}$; and $4 \times 10^{-9} \leqslant CO_2 \leqslant 7 \times 10^{-8}$. However, in considering the $\xi^2 = 1$ surface, we might be overinterpreting the data.

We find definitive detections of CH_4, CO, and CO_2. Even at the $\xi^2 = 4$ surface, the data require non-zero mixing ratios for the carbon-bearing molecules. Furthermore, the results suggest a high C/O ratio (see Seager et al. 2005). Although the model fits give C/O ratio close to 1 or higher, our molecular abundance grid resolution is not high enough to put a precise lower limit to the C/O ratio. As seen from Figure 10, the allowed models reach values as high as ~60 for $\xi^2 = 1$, and ~600 for $\xi^2 = 2$. As discussed previously, and in Section 6.1, high molecular concentrations and high C/O ratios could be localized effects overrepresented by the 1D averaged retrieval.

5.2. Temperature Structure

The most interesting aspect about the atmosphere of HD 209458b is the presence of a thermal inversion on the planet dayside, as previous studies have pointed out (e.g., Burrows et al. 2008). While modeling atmospheric spectra, one often encounters a degeneracy between temperature structure and molecular compositions. However, by exploring a large number of P–T profiles we find that the dayside observations for HD 209458b cannot be explained without a thermal inversion, for any chemical composition, at the $\xi^2 < 2$ level. On the other hand, our results place stringent constraints on the 1D averaged structure of the required thermal inversion.

Our results presented here explore ~7000 P–T profiles with thermal inversions. Figure 11 shows all the P–T profiles with

$\xi^2 \leqslant 5$. The ranges in the P–T parameters explored are shown in Figure 10. In the presence of a thermal inversion, the spectra are dominated by the location and extent of the inversion layer, quantified by the parameters P_2, T_2, and α_2. We find the models with $\xi^2 \leqslant 2$ to have an inversion layer in the lower atmosphere, at pressures (P_2) above ~0.03 bar, with the best-fit models preferring the deeper layers, i.e., higher P_2. We find that the $\xi^2 \leqslant 1$ region extends to inversion layers as deep as $P_2 \sim 1$ bar. However, we limit P_2 to a value of 0.5 based on the physical consideration that, at pressure $\gtrsim 1$ bar collisional opacities are likely to dominate over the molecular opacities in the optical which are expected to be the cause of thermal inversions. And, therefore, we do not expect inversions at such high pressures.

The allowed models (Figure 10) cover a wide range in the base temperature (T_3) owing to the fact that the spectrum is dominated by the maximum temperature differential ($T_1 - T_2$) attained in the stratosphere, and is less sensitive to T_3 by itself. The stratospheric temperatures of all the models with $\xi^2 \leqslant 2$ lie between 800 K and 2200 K. The temperature gradient in the inversion layer is governed by the α_2 parameter. As can be seen from Figure 10, the data restrict the $\xi^2 \leqslant 2$ models to have α_2 between 0.05 and 0.25, with the $\xi^2 \leqslant 1$ models preferring values between 0.05 and 0.15. These values of α_2 translate into mean temperature gradients ($< dT/d \log P >$) in the inversion layer to be 230–1480 K for $\xi^2 \leqslant 2$, and 400–1480 K for $\xi^2 \leqslant 1$. Consequently, large thermal inversions spanning more than a few dex in pressure, and hence with less steeper thermal gradients, are ruled out by the data. This is also evident from Figure 11. Finally, ξ^2 is not very sensitive to the parameters in Layer 1 of the P–T profile, since the dominant spectral features in this planet arise from the inversion layer.

5.3. Albedo and Energy Redistribution

Our results also show the constraints on the albedo and day–night redistribution. Figure 10 shows the ξ^2 surface in the space of T_{eff} versus η, where, $\eta = (1 - A_B)(1 - f_r)$; A_B is the Bond albedo, and f_r is the fraction of input stellar flux redistributed to the night side. As described in Section 4.1.3, using η one can estimate the constraint on A_B given f_r, or vice versa. For HD 209458b, the $\xi^2 = 2$ surface in Figure 10 constrains η in the range 0.24–0.81, with the $\xi^2 = 1$ surface in the range 0.26–0.72. If we assume an A_B of 0.24 (2σ upper limit, scaled from the 1σ estimate of Rowe et al. 2008), the constraints on f_r for the $\xi^2 = 2$ and $\xi^2 = 1$ surfaces are 0.0–0.68 and 0.05–0.66, respectively. This range of values allows for very efficient redistribution in the atmosphere of HD 209458b, although values of $f_r > 0.5$ seem physically unrealistic.

6. DISCUSSION

Our results in this work have been presented as goodness-of-fit contours in the parameter space of a 1D averaged atmosphere model. In this section, we first discuss the interpretation of our results in the light of the fact that the atmosphere is inherently 3D, with dynamical effects that cannot be captured in a 1D model. We then present an assessment of our best-fit models vis-a-vis the goodness-of-fit contours. Finally, we discuss possible future extensions to our model.

6.1. Contribution Functions

We have constrained the P–T profile and abundances on the planetary dayside. But which part of the atmosphere is really being sampled by the observations? Here, we will discuss

the contribution to the net emergent flux from the surface elements at the top of the atmosphere (see Knutson et al. 2009a for a discussion of radial contribution functions). We begin with the simple picture of radiative equilibrium, with no atmospheric circulation, in a homogeneous and isotropically radiating atmosphere. In this case, the amount of flux from a given surface element is proportional to the amount of incident flux from the star, where the incident stellar flux drops off as $\cos\theta$; θ is the angle away from the substellar point. In this picture, the planetary infrared flux is greatest at the substellar point, where the planet is being heated the most. The area contribution to the net planet flux, however, increases as $\sin\theta$. The bigger annuli correspond to larger areas on the projected planetary disk as viewed by the observer. The lower flux emitting regions (the outer regions of the disk, with lower incident stellar intensity), therefore, have more area than the higher flux regions. There is a sweet spot at 45 deg where the contribution to the total observed flux peaks, with a distribution of $\sin(2\theta)$. In other words, the total flux is an average over a wide region on the projected planetary disk.

A more realistic scenario is one not limited to radiative equilibrium; indeed atmospheric circulation models show dramatic differences of emergent flux across the planetary disk caused by strong hydrodynamic flows (see, e.g., Showman et al. 2009; Langton & Laughlin 2008; Cho et al. 2003; Dobbs-Dixon & Lin 2008). Without knowing the atmospheric circulation and the resulting surface pattern, can we say anything about which part of the dayside planetary disk our P–T profiles and abundances preferentially sample? Given a retrieved abundance for a molecule, we do not know if this is from a localized concentration or from a global abundance, or something in between. For instance, we have found evidence for a high CO_2 abundance in HD 189733 (see also Swain et al. 2009a). But is this just a local effect of transported photochemical products? Or is the whole dayside evenly enriched in CO_2? If we are not measuring a true average, we have to be careful about how we interpret the retrieved CO_2 abundance.

A thorough examination of the contribution of different parts of the planetary disk has to take into account the emergent surface flux profiles that are more realistic than the assumption of homogeneity and radiative equilibrium. For example, 3D models of hot Jupiter atmospheres by Showman et al. (2009) show a much slower than $\cos\theta$ drop off from the substellar point caused by hydrodynamic flows. And at the planetary photosphere the "substellar hot spot" is blown downwind, to 30 deg; a detail that would not be apparent in the assumption of an isotropic and homogenous atmosphere. Moreover, the *Spitzer* 8 micron measurements by Knutson et al. (2007) show a hot spot at lower separation from the substellar point (and also show a cold spot on the same hemisphere). For instance, if CO_2 were predominantly formed in localized regions and blown downwind, it could land at geometrically favored regions in terms of the 1D averaged spectrum. Alternatively, vertically localized concentrations of CO_2 at favorable pressure levels could give rise to strong spectral signatures, similar to those formed by having the same concentration of CO_2 over the entire atmosphere. In these cases, a high value of CO_2 may not be representative of the entire dayside.

6.2. Best-fit Models Versus Error Surface

In the current work, we have described most of our results at the $\xi^2 = 2$ level. Our formulation for ξ^2, as described in Section 3.5, would be equivalent to the conventional definition of reduced χ^2, if N_{obs} were to be replaced by the number of degrees of freedom. Normally, one aims for fits at the reduced $\chi^2 = 1$ level (we have also provided results for fits at the level of $\xi^2 = 1$). A χ^2, however, is devoid of meaning when the number of degrees of freedom is less than zero—in that we cannot relate χ^2 to a confidence level. In the absence of confidence levels, we are considering ξ^2 as a weighted mean squared error. In this framework, a $\xi^2 = 1$ means that, on average, the model deviates from the mean values of the data by 1σ, and $\xi^2 = 2$ means that the deviation is $\sqrt{2} = 1.4\sigma$. In this work, the number of data points in the *Spitzer* broadband photometry is less than the number of free model parameters, meaning less than zero degrees of freedom. In both the *Spitzer* IRS and the *HST*/NICMOS data sets, there are, in principle, more data points than the number of free model parameters. But both these data sets sample a narrow wavelength range, with a limited number of absorption features. In addition, the degeneracies in our model parameter space are poorly understood, if at all. Without a robust parameter-fitting algorithm, we cannot assign confidence levels even with the *HST* and IRS data sets. Which error surface should be used to encompass the best-fit models, given that we have no direct correspondence to confidence levels? There is no conclusive answer and, ideally, one might like to consider only those models which fit the data to within $\xi^2 = 1$, or even $\xi^2 = 0$ indicating perfect fits. However, we have used a conservative choice of the $\xi^2 = 2$ surface for interpretation of our results, allowing for models fitting the observations to within $\sim 1.4\sigma$ of each data point, on an average.

One approach to accurately consider the uncertainty on the data is as follows. One could take tens of thousands of realizations of each data set, uniformly sampled over the error distribution. Fitting each realized data set would mean running millions of models for each case, leading up to billions of models per data set per planet. Such an approach is computationally prohibitive at the present time.

6.3. Suggested Variability

There is evidence that the dayside atmosphere of HD 189733b is variable. One highly relevant example to our interpretation is the 8 μm *Spitzer* IRAC measurement of HD 189733b reported by Knutson et al. (2007) versus that reported by Charbonneau et al. (2008) in the same channel at a different time. The flux ratios differ by $\sim 2.3\sigma$. Also significant is the disagreement in the planet-star contrast levels between the HD 189733b IRS spectrum and the IRAC broadband photometry at 8 μm, but not at 5.8 μm (Grillmair et al. 2008).

Atmospheric variability is also suggested by the very strong CO_2 feature in the HD 189733 *HST*/NICMOS data set and the lack of a noticeably strong absorption feature in the 4.5 μm and 16 μm *Spitzer* channels. It is well known that the CO_2 molecule has an extremely strong absorption feature at 15 μm; yet there is no indication of strong CO_2 absorption observed in the 16 μm channel. Whether this data variability is due to intrinsic variability of the planet atmosphere or instead is due to the different data reduction techniques is under study (Desert et al. 2009; Beaulieu et al. 2009).

Turning to our model results, we have been unable to find fits to all three data sets of HD 189733b at the $\xi^2 \leqslant 2$ level, in the large range of parameter space we have explored. There may be befitting P–T profiles and compositions that our grid did not cover, but we think this is unlikely, mainly because the data sets show noticeable differences even without running the models, e.g., the observed features of CO_2. We plan to implement a more

exhaustive exploration of the P–T parameter space by extending our work with a new optimization technique in the future.

6.4. Model Extensions

Our approach allowed us to run a large ensemble of models in the parameter space. Nevertheless, future calculations are needed to estimate the covariances between the model parameters. Several model parameters are degenerate; for example, molecular abundances of species that share absorption features in the same photometric channel (e.g., CO and CO_2). Also well-known is the degeneracy between the P–T profile and the molecular abundances. Understanding the covariances between the parameters might help break the degeneracies in the future.

We chose the $\sim 10^4$ P–T profiles based on physical arguments and preliminary fits to the data. Even though having a grid of $\sim 10^4$ P–T profiles in the six-parameter P–T space, and $\sim 10^7$ models overall, means that our grid is coarse, we believe it covers most physically plausible profiles. Nonetheless, a more complete exploration requires a more sophisticated approach, and may find P–T profiles and the corresponding abundance constraints that may be slightly different from those reported here.

Our model does not include clouds or scattering. Although cloudless models are justified for hot Jupiters (see Section 3.2), clouds are needed for extending our model to cooler planetary atmospheres, such as those of habitable zone super Earths and cooler giant planets. Our model also does not include photochemistry, but instead varies over different molecular abundances. Once a set of best-fit models are found by our approach, the molecular abundances can be used to guide photochemical models; conversely, photochemical models can be used to check the plausibility of the best-fit molecular abundances. And, although we have used the latest available high-temperature opacities, further improvements are sought, particularly for CH_4 and CO_2.

Our model presented in this work is suitable only for interpreting the infrared spectra of planetary atmospheres; it was motivated by existing observations. We do not include the sources of opacity and scattering that are required to model the visible part of the spectra. However, our model can be extended to visible wavelengths, and we aim to discuss it in a future work. Constraints placed by visible observations will help to further narrow down the model parameter space already constrained by IR observations.

We have not included the intrinsic flux from the planet interior, because, for hot Jupiters stellar irradiation is the dominant energy source. However, extensions of our model to brown dwarf atmospheres or young, or massive, Jupiters will require inclusion of the interior energy. And, although irradiation is naturally included in the form of the parametric P–T profile, our model gives no information about the nature of the absorber. Nevertheless, given the best-fit P–T profile from our approach, one could quantify the range of parameters of a potential absorber.

6.5. Temperature Retrieval as a Starting Point for Forward Models

We have presented a radical departure from the standard exoplanet atmosphere models. Our temperature and abundance retrieval method does not use the assumption of radiative + convective equilibrium in each layer to determine the P–T profile. By searching over millions of models, we are extracting the P–T profile from the data.

We have not necessarily suggested to replace the so-called self-consistent forward models, those models that include radiative transfer, hydrostatic equilibrium, radiative + convective equilibrium, day–night energy redistribution, non-equilibrium chemistry, and cloud formation. Instead of a stand-alone model, our method can be used as a starting point for narrowing the potential parameter space to run forward models in. We anticipate that this temperature retrieval method will enable modelers to run enough forward models to find quantitative constraints from the data, instead of running only a few representative models.

Atmospheric temperature and abundance retrieval is not new. Solar system planet atmosphere studies use temperature retrieval methods, but in the present context there is one major difference. Exquisite data for solar system planet atmospheres means that a fiducial P–T profile can be derived. The temperature retrieval process for a solar system planet atmosphere therefore involves perturbing the fiducial profile. For exoplanets, there is no starting point to derive a fiducial model because of the limited data. Building on methods used for solar system planets, Swain et al. (2008b, 2009b) have used a temperature retrieval method using published P–T profiles from other models, and perturbing the profiles to find fits to data (also see Sing et al. 2008). In this work, we report a new approach for atmospheric retrieval of exoplanets which allows us to explore a wide region of the parameter space, and to possibly motivate a new generation of retrieval methods tailored to exoplanet atmospheres.

7. SUMMARY AND CONCLUSIONS

We have presented a solution to the retrieval problem in exoplanet atmospheres: given a set of observations, what are the constraints on the atmospheric properties? Our method consists of a new model involving line-by-line radiative transfer with a parametric P–T profile, along with physical constraints of hydrostatic equilibrium and global energy balance, and allowing for non-equilibrium molecular compositions. This approach enabled us to run millions of models of atmospheric spectra over a grid in the parameter space, and to calculate goodness-of-fit contours for a given data set. Thus, given a set of observations and a desired measure of fit, our method places constraints on the P–T profile and the molecular abundances in the atmosphere.

We used our method to place constraints on the atmospheric properties of two hot Jupiters with the best available data: HD 189733b and HD 209458b. We computed $\sim 10^7$ models for each system. Our constraints on the P–T profiles confirm the presence of a thermal inversion on the dayside of HD 209458b, and the absence of one in HD 189733b, as has been previously reported in the literature. And, the constraints on molecular abundances confirm the presence of H_2O, CH_4, CO, and CO_2 in HD 189733b, as has been found by several other studies in the past.

We presented some new findings. We report independent detections of H_2O, CH_4, CO_2, and CO, from six-channel *Spitzer* photometry, at the $\xi^2 < 1$ level (see also Swain et al. 2009b). At the $\xi^2 = 2$ surface, we find the lower limits on the mixing ratios of CH_4, CO, and CO_2 to be 10^{-8}, 4×10^{-5}, and 2×10^{-9}, respectively. In addition, we find an upper limit on H_2O mixing ratio of 10^{-4}. Second, our results using the high S/N IRS spectrum of HD 189733b indicate that the best-fit models are consistent with efficient day–night circulation on this planet, consistent with the findings of Knutson et al. (2007, 2009a); although, we also find that the broadband photometry data require much less efficient day–night circulation, as has been reported by several studies in the past. The different constraints

placed by the different data sets arise from the variability in the data.

A few key observations of HD 189733b vary between different data sets at similar wavelengths. Moreover, a noticeably strong CO_2 absorption in one data set is significantly weaker in another. We must, therefore, acknowledge the strong possibility that the atmosphere is variable, both in its energy redistribution state and in the chemical abundances.

Our new temperature and abundance retrieval—together with the limited but remarkable data sets—charts a new course for exoplanet atmosphere interpretation. Whether our approach is used as a stand-alone model, or as a starting point for forward models, the field of exoplanet atmospheres is ready for a technique to place detailed atmospheric constraints governed by the data. The ideal data set is one with a wide wavelength range that covers more than one spectral feature of different molecules. The *James Webb Space Telescope*, scheduled for launch in 2013, is ideal for observations of transiting exoplanet atmospheres and should usher a new era for quantitative analyses of exoplanet atmospheres.

REFERENCES

Barman, T. S. 2007, ApJ, 661, L191
Barman, T. S. 2008, ApJ, 676, L61
Barman, T. S., Hauschildt, P. H., & Allard, F. 2005, ApJ, 632, 1132
Barnes, J. R., et al. 2007, MNRAS, 382, 473
Beaulieu, J. P., Carey, S., Ribas, I., & Tinetti, G. 2008, ApJ, 677, 1343
Beaulieu, J. P., et al. 2009, arXiv:0909.018
Borysow, A. 2002, A&A, 390, 779
Borysow, A., Jorgensen, U. G., & Zheng, C. 1997, A&A, 324, 185
Burrows, A., Budaj, J., & Hubeny, I. 2008, ApJ, 678, 1436
Burrows, A., Hubeny, I., Budaj, J., Knutson, H. A., & Charbonneau, D. 2007, ApJ, 668, L171
Burrows, A., Sudarsky, D., & Hubeny, I. 2006, ApJ, 650, 1140
Burrows, A., & Sharp, C. M. 1999, ApJ, 512, 843
Castelli, F., & Kurucz, R. L. 2004, arXiv:astro-ph/0405087v1
Charbonneau, D., Brown, T. M., Noyes, R. W., & Gilliland, R. L. 2002, ApJ, 568, 377
Charbonneau, D., et al. 2008, ApJ, 686, 1341

Cho, J. Y.-K., Menou, K., Hansen, B. M. S., & Seager, S. 2003, ApJ, 587, L117
COESA (Committe on Extension to the Standard Atmosphere) 1976, U.S. Standard Atmosphere (Washington, DC: Government Printing Office)
Cooper, C. S., & Showman, A. P. 2006, ApJ, 649, 1048
Deming, D., Harrington, J., Seager, S., & Richardson, L. J. 2006, ApJ, 644, 560
Deming, D., Seager, S., Richardson, L. J., & Harrington, J. 2005, Nature, 434, 740
Desert, J.-M., et al. 2009, ApJ, 699, 478
Dobbs-Dixon, I., & Lin, D. N. C. 2008, ApJ, 673, 513
Fortney, J. J., Lodders, K., Marley, M. S., & Freedman, R. S. 2008, ApJ, 678, 1419
Fortney, J. J., Saumon, D., Marley, M. S., Lodders, K., & Freedman, R. S. 2006, ApJ, 642, 495
Freedman, R. S., Marley, M. S., & Lodders, K. 2008, ApJS, 174, 504
Goody, R. M., & Yung, Y. L. 1989, Atmospheric Radiation (New York, NY: Oxford Univ. Press)
Grillmair, C. J., et al. 2008, Nature, 456, 767
Knutson, H. A., Charbonneau, D., Allen, L. E., Burrows, A., & Megeath, S. T. 2008, ApJ, 673, 526
Knutson, H. A., et al. 2007, Nature, 447, 183
Knutson, H. A., et al. 2009a, ApJ, 690, 822
Knutson, H. A., et al. 2009b, ApJ, 691, 866
Langton, J., & Laughlin, G. 2008, arXiv:0808.3118
Levenberg, K. 1944, Quart. Appl. Math., 2, 164
Liang, M.-C, Parkinson, C. D., Lee, A. Y.-T., Yung, Y. L., & Seager, S. 2003, ApJ, 596, L247
Lindal, G. F., et al. 1981, J. Geophy. Res., 86, 8721
Lindal, G. F., et al. 1985, AJ, 90, 1136
Lindal, G. F., et al. 1987, J. Geophy. Res., 92A, 14987
Lindal, G. F., et al. 1990, Geophys. Res. Lett., 17, 1733
Marley, M. S., et al. 2002, ApJ, 568, 335
Marquardt, D. 1963, SIAM J. Appl. Math., 11, 431
Pont, F., Knutson, H., Gilliland, R. L., Moutou, C., & Charbonneau, D. 2008, MNRAS, 385, 109
Redfield, S., Endl, M., Cochran, W. D., & Koesterke, L. 2008, ApJ, 673, L87
Richardson, L. J., Deming, D., Horning, K., Seager, S., & Harrington, J. 2007, Nature, 445, 892
Richardson, L. J., Deming, D., & Seager, S. 2003, ApJ, 597, 581
Rothman, L. S., et al. 2005, J. Quant. Spec. Radiat. Transfer, 96, 139
Rowe, J. F., et al. 2008, ApJ, 689, 1345
Seager, S., Deming, D., & Valenti, J. A. 2008, Astrophysics in the Next Decade: JWST and Concurrent Facilities, Astrophysics & Space Science Library (Dordrecht: Springer)
Seager, S., Richardson, L. J., Hansen, B. M. S., Menou, K., Cho, J. Y.-K., & Deming, D. 2005, ApJ, 632, 1122
Showman, A. P., Fortney, J. J., Lian, Y., Marley, M. S., Freedman, R. S., Knutson, H. A., & Charbonneau, D. 2009, ApJ, 699, 564
Sing, D., et al. 2008, ApJ, 686, 667
Spiegel, D. S., Silverio, K., & Burrows, A. 2009, ApJ, 699, 1487
Swain, M. R., Bouwman, J., Akeson, R. L., Lawler, S., & Beichman, C. A. 2008a, ApJ, 674, 482
Swain, M. R., Vasisht, G., & Tinetti, G. 2008b, Nature, 452, 329
Swain, M. R., et al. 2009a, ApJ, 690, L114
Swain, M. R., et al. 2009b, ApJ, 704, 1616
Tinetti, G., et al. 2007, Nature, 448, 169
Torres, G., Winn, J. N., & Holman, M. J. 2008, ApJ, 677, 1324
Zahnle, K., Marley, M. S., Lodders, K., & Fortney, J. J. 2009, ApJ, 701, L20